Ultrasound in Med. & Biol., Vol. 48, No. 1, pp. 98–110, 2022

0301-5629/$ - see front matter

https://doi.org/10.1016/j.ultrasmedbio.2021.09.008

● *Original Contribution*

TRANSCRANIAL MAGNETIC RESONANCE-GUIDED HISTOTRIPSY FOR BRAIN SURGERY: PRE-CLINICAL INVESTIGATION

Ning Lu,* Dinank Gupta,* Badih J. Daou,† Adam Fox,* Dave Choi,* Jonathan R. Sukovich,* Timothy L. Hall,* Sandra Camelo-Piragua,‡ Neeraj Chaudhary,†,§ John Snell,¶ Aditya S. Pandey,†,§ Douglas C. Noll,*,[2] and Zhen Xu*,[2]

* Department of Biomedical Engineering, University of Michigan, Ann Arbor, Michigan, USA; † Department of Neurosurgery, University of Michigan, Ann Arbor, Michigan, USA; ‡ Department of Pathology, University of Michigan, Ann Arbor, Michigan, USA; § Department of Radiology, University of Michigan, Ann Arbor, Michigan, USA; and ¶ Focused Ultrasound Foundation, Charlottesville, Virginia, USA

(*Received* 14 *May* 2021; *revised* 30 *August* 2021; *in final form* 6 *September* 2021)

Abstract—Histotripsy has been previously applied to target various cranial locations *in vitro* through an excised human skull. Recently, a transcranial magnetic resonance (MR)-guided histotripsy (tcMRgHt) system was developed, enabling pre-clinical investigations of tcMRgHt for brain surgery. To determine the feasibility of *in vivo* transcranial histotripsy, tcMRgHt treatment was delivered to eight pigs using a 700-kHz, 128-element, MR-compatible phased-array transducer inside a 3-T magnetic resonance imaging (MRI) scanner. After craniotomy to open an acoustic window to the brain, histotripsy was applied through an excised human calvarium to target the inside of the pig brain based on pre-treatment MRI and fiducial markers. MR images were acquired pre-treatment, immediately post-treatment and 2–4 h post-treatment to evaluate the acute treatment outcome. Successful histotripsy ablation was observed in all pigs. The MR-evident lesions were well confined within the targeted volume, without evidence of excessive brain edema or hemorrhage outside of the target zone. Histology revealed tissue homogenization in the ablation zones with a sharp demarcation between destroyed and unaffected tissue, which correlated well with the radiographic treatment zones on MRI. These results are the first to support the *in vivo* feasibility of tcMRgHt in the pig brain, enabling further investigation of the use of tcMRgHt for brain surgery. (E-mail: zhenx@umich.edu)

Key Words: **Histotripsy, Magnetic resonance imaging, Transcranial treatment, Therapeutic ultrasound, Brain.**

INTRODUCTION

Non-invasive techniques are ideal for the treatment of brain pathologies to prevent risks associated with incisions, cranial exposure and manipulation, as well as penetration of healthy intervening tissue. Transcranial magnetic resonance-guided focused ultrasound (tcMRgFUS) has been investigated as an emerging treatment option alternative to surgical resection and radiosurgery for brain diseases (Martin et al. 2009; McDannold et al. 2010; Alkins et al. 2013; Monteith et al. 2013; Coluccia et al. 2014; Aubry and Tanter 2016; Federau et al. 2018; Lipsman et al. 2018). Under magnetic resonance imaging (MRI) guidance, tcMRgFUS is applied through the intact skull and focused on the target brain tissue to produce thermal necrosis without damaging the peripheral tissue. Commercial tcMRgFUS systems have been approved by the U.S. Food and Drug Administration (FDA) to ablate a single focal volume in the central nervous system as a therapy for essential tremors (Elias et al. 2013; Lipsman et al. 2013; Federau et al. 2018). Studies using tcMRgFUS to treat Parkinson's diseases and brain tumors are also currently ongoing (McDannold et al. 2010; Coluccia et al. 2014; Fasano et al. 2018; Ji et al. 2019). However, the tcMRgFUS technology available today has several limitations preventing its broad application to brain pathologies. As the skull bone highly attenuates the ultrasound beam, it is challenging to use tcMRgFUS to treat locations outside the central region of the brain without overheating the skull, leaving it unusable for common pathologies that arise near the surface of the brain (Martin et al. 2009;

Address correspondence to: Zhen Xu, University of Michigan, 2200 Bonisteel Boulevard, Ann Arbor, MI 48109, USA. E-mail: zhenx@umich.edu

[2] Douglas C. Noll and Zhen Xu are both senior authors for this manuscript.

McDannold et al. 2010; Pulkkinen et al. 2011; Arvanitis et al. 2016). This peri-target heating also limits the treatment rate of tcMRgFUS for large-volume targets, leading to a longer treatment time that may be impractical for larger ablation volumes (McDannold et al. 2010; Arvanitis et al. 2016).

Various solutions have been investigated to reduce the skull heating and widen the treatment envelope for transcranial focused ultrasound, including the use of lower ultrasound frequencies (Behrens et al. 1999; Xu et al. 2015), incorporation of ultrasound enhancing agents (Arvanitis et al. 2016) and rearrangement of transducer position and geometry. The combination of low-intensity ultrasound bursts and an intravenously administered microbubble agent has been presented to treat targets near the skull base with a much lower acoustic exposure level to effectively mitigate skull heating (Arvanitis et al. 2016). However, the cavitation from microbubbles produced unfocused, patchy ablation zones with discrete necrotic areas intermixed with surviving neurons and generated prefocal lesions outside of the target zone.

Unlike tcMRgFUS, which relies on heating produced by continuous sonication, histotripsy uses short (several-microsecond), high-pressure ultrasound pulses (>26 MPa) to generate focused cavitation bubbles with no need for any external nucleation agents (Xu et al. 2004; Khokhlova et al. 2015). The rapid expansion and collapse of generated bubble clouds produce localized strain in tissue to mechanically fractionate and liquefy the targeted volume into homogenized acellular debris (Parsons et al. 2006). Because the damage generated by histotripsy is confined within the regions where the pressure exceeds the intrinsic threshold for nucleation, histotripsy is robust even when aberrations are caused by a heterogeneous medium in the path of its transmission such as the human skull (Kim et al. 2014; Sukovich et al. 2016). The cavitation bubble cloud produces a sharp margin between destroyed and unaffected tissue, leading to high ablation precision with minimal damage to surrounding tissues. Moreover, short ultrasound pulses used by histotripsy lead to duty cycles <0.1% with long cooling time between pulses, allowing transcranial histotripsy to effectively ablate the target tissue with reduced heating of the skull and surrounding tissue. Prior studies have determined that histotripsy can liquefy up to 40 mL of a clot within 20 min through the excised human skull at varying cranial depths while maintaining a temperature increase in the skull <4°C (Gerhardson et al. 2017). To address the concern that histotripsy may cause excessive hemorrhage or edema in the brain, an initial *in vivo* study was performed and found that cerebral lesions can be generated in the normal pig brain without excessive bleeding in the acute or subacute phases after treatment (Sukovich et al. 2019). However, for this initial study, histotripsy was applied to the pig brain after a craniotomy, because the pig skull is too thick for effective ultrasound penetration. These preliminary results suggested the potential of using histotripsy for non-invasive transcranial brain surgery for varying sizes and locations of cerebral pathology.

Because histotripsy-generated cavitation can be visualized on ultrasound imaging, histotripsy treatment is typically guided by ultrasound imaging (Wang et al. 2009; Vlaisavljevich et al. 2013). However, transcranial ultrasound imaging remains challenging without contrast agents. MRI, in comparison, offers high resolution and contrast to visualize anatomical structures for identifying treatment targets. The signal intensity changes induced by histotripsy on MR images also correlate well with histopathological changes, thus providing information for treatment monitoring and outcome evaluation. Therefore, to develop transcranial histotripsy for brain surgery, MR guidance as an adjunct modality is an essential tool to ensure treatment efficacy and precision.

Recently, the first transcranial MR-guided histotripsy (tcMRgHt) system was designed and constructed in our laboratory, enabling the first pre-clinical investigations on tcMRgHt treatment (Lu et al. 2021). The primary goals of the present study were (i) to determine the *in vivo* feasibility of using tcMRgHt to treat targets in different locations in the pig brain through an excised human calvarium; (ii) to evaluate the acute treatment outcome (within 4 h post-treatment) based on MR imaging correlated with histopathology; and (iii) to gain knowledge on initial targeting accuracy and safety of tcMRgHt for brain surgery and shed light on potential improvements for tcMRgHt.

METHODS

Animals

This study was approved by the Institutional Animal Care and Use Committee at the University of Michigan. Twelve male and female juvenile pigs weighing 27−37 kg underwent anesthetization procedures at the animal surgery and operating room. The pigs' scalps were carefully shaved in an attempt to prevent air bubbles from being trapped in the hair during later histotripsy treatment. A vertical incision was drawn from the anterior aspect to the posterior aspect of the swine skull. After prepping and draping in a sterile fashion, a craniotomy was performed to remove a 60-mm-diameter circular region of the calvarium while keeping the dura intact. This was performed to minimize the acoustic attenuation induced by the pig skull, which is much thicker compared with a human skull. The craniotomy site was irrigated with large amounts of sterile phosphate-buffered saline solution (0.9% sodium chloride,

Hospira, Lake Forest, IL, USA). Then, the skin was sutured, and saline was injected under the skin flap to fill the vacant space to expel gases. Because residual air bubbles would significantly degrade ultrasound transmission through the acoustic opening, pigs were recovered for 2 d before histotripsy treatment to allow for the dissolution of any air trapped under the incision. Four pigs were used as pilot subjects to test the device, the experimental setup and the treatment workflow, and were not counted in the treatment group. The subsequent eight pigs underwent transcranial histotripsy treatment and went through all pre- and post-imaging scans in a clinical 3-T MRI scanner (Discovery MR750, GE Healthcare, Milwaukee, WI, USA) in the Functional MRI Laboratory at our university.

Skull preparation

Given the goal of transcranial treatment, an excised human calvarium was placed over the acoustic window created by craniotomy. The calvarium was obtained from the Institutional Anatomical Donations Program, de-fleshed after extraction, fixed in formalin and preserved in water thereafter. Before all treatments, the calvarium was de-gassed in water inside a vacuum chamber for a minimum of 6 h. The dimensions of the human calvarium were 158 mm on the anterior-to-posterior axis, 139 mm on the mediolateral axis and 56 mm in depth from the interior surface to the cut plane of the skull. The minimal and maximal thicknesses of the calvarium were 2.5 and 8.5 mm, respectively.

Device and experimental setups

The device used in this study was a 700-kHz, 360-element MR-compatible hemispherical array developed in-house. The transcranial transducer array was originally designed based on the dimension of human-scale subjects with a radius of 150 mm. We populated only the inner 128 elements of the full array scaffold for this swine study, as the other transducer elements located on the outer portion of the hemispherical array would be blocked by the remaining pig skull. This 128-element array had an effective *f*-number (focal distance/aperture diameter) of 0.74. The array was constructed using 3-D-printed and acetal materials to minimize the mass of metal, thus ensuring MR safety and good image quality. Driving electronics for the transducer array were placed in an adjacent control room and connected to the array via micro-coaxial cables and high-density connectors.

The 128-element tcMRgHt array was estimated to generate a peak negative pressure ($p\_$) up to 137 MPa in the free field and 48.4 MPa through the calvarium in water without aberration correction (Lu et al. 2021). The heterogeneous thickness and composition of the skull bone cause attenuation and phase aberration to the ultrasound beam, which distorts the focus and limits the efficacy of transcranial histotripsy treatment. To compensate for the skull-induced phase aberration, pressure waveforms were acquired from individual transducer elements through the skull using a needle hydrophone for each treatment before the pig was placed within the transducer. These signals were cross-correlated to a single reference signal, and the associated correlation delays were applied as offsets to the elements' firing times to align the pulses at the focus. With the skull aberration compensated, the tcMRgHt array was estimated to provide a $p\_$ up to 72 MPa through the calvarium in water. The electronic focal steering range through the skull where peak negative pressures >26 MPa could be achieved to generate cavitation was found to be 33.5 mm laterally and 50 mm axially (Lu et al. 2021), offering sufficient acoustic power for volume target treatment.

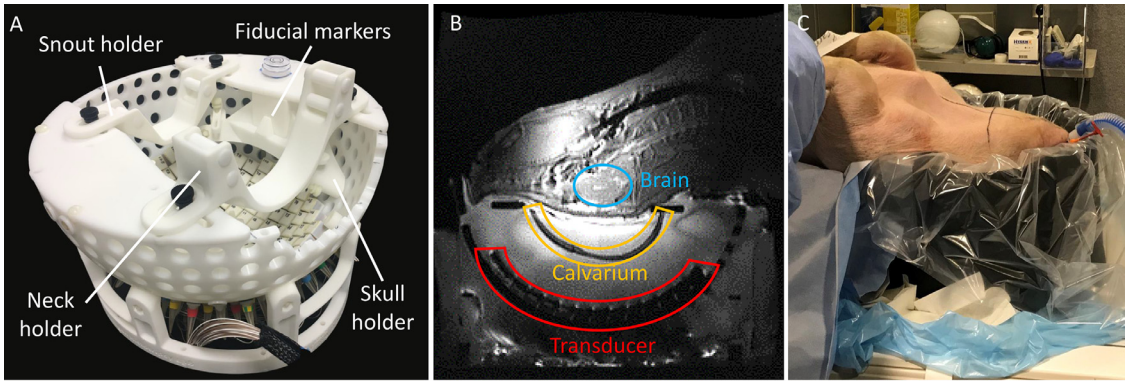

Fig. 1. Device and experimental setups. (a) Photograph of the assembled transcranial magnetic resonance-guided histotripsy (tcMRgHt) array with supporting structures. (b) MR localizer image of the experimental setup during *in vivo* pig treatment from the sagittal view. The locations of the transducer, the excised human calvarium and the pig brain were labeled on the image. (c) Photograph of the pig in position for tcMRgHt treatment. With the tcMRgHt array placed on the MR bed, the pig was placed supine on a V-tray with its head supported by the snout and neck holder on the tcMRgHt array. The head was partially submerged in de-gassed saline with the fluid level aligned with the pig's eyes for acoustic coupling.

To facilitate the *in vivo* transcranial pig treatment, support structures including fiducial markers, a skull holder, a snout holder and a neck holder were fabricated using 3-D-printed materials (Fig. 1a). The fiducial markers were mounted rigidly to the array scaffold to provide reference points for targeting. The skull holder was used to mount the excised human calvarium inside the array scaffold at a fixed position and orientation during treatment. The snout and neck holders were designed based on empirical measurements from the pilot pigs. During treatment, the whole assembly was placed in a waterproof canvas bag on the MRI bed and immersed in de-gassed saline for acoustic coupling. A spirit level was mounted on top of the histotripsy array to check the horizontal level.

The experimental setup for tcMRgHt is illustrated in Figure 1. The pig was placed supine on a V-tray with its head supported by the snout and neck holders. The pig head was positioned in the appropriate location and orientation to ensure the desired brain target would lie within the electronic steering range for optimal treatment efficacy. The head was partially submerged in de-gassed saline at room temperature with the fluid level aligned with the pig's eyes. The pigs were maintained under general anesthesia with vital signs monitored during the entire treatment procedure, including pre- and post-treatment imaging. Three heated circulating water blankets were used to maintain normal body temperature.

Transcranial histotripsy treatment

Histotripsy treatment was applied through the excised human calvarium, targeting a single volume in each pig. The targeted anatomical locations and treatment parameters for each pig are summarized in Table 1. Deep regions were targeted in 6 pigs (*e.g.,* basal ganglia) and superficial regions were targeted in 2 pigs (*i.e.,* cortical gray-white matter). For each volume target, locations in a cubic grid were treated by electronic focal steering with 1−2 mm between adjacent focal locations. The planned treatment zones ranged in volume from 40.5−450 mm^3. These relatively small target volumes were selected because of the small size of the pig brain. Previously, Sukovich et al. (2019) reported that the extent of cellular damage within a focal volume was observed to increase with dose in an intracranial *in vivo* study, where ≥50 pulses per location resulted in ≥90% destruction of the tissue within the focal volume. Therefore, we chose to deliver 50 pulses to each focal location at a pulse repetition frequency of 10 Hz. The electronic focal steering scanning sequence, generated as a raster pattern, was randomized before the treatment because previous studies have suggested that randomly ordering the temporal sequence of focal sites in a volume ablation fractionates tissue more effectively than using a raster scan by reducing the cavitation memory effect (Lundt et al. 2017). Such a randomized pattern was then repeated 50 times to complete the volume treatment. Skull-induced aberration was not compensated for the first three pig treatments, leading to an estimated p_- of 48.4 MPa at the geometric focus. The other five pigs were treated with a higher estimated peak negative pressure of 72 MPa at the geometric focus with aberration correction using the hydrophone. It should be noted that pig 5 underwent histotripsy treatment twice at the same location because no obvious change was observed on MRI after the first treatment, resulting in a doubled dose (100 pulses).

Magnetic resonance imaging

For all MRI scans, a body coil was used for transmission, whereas a pair of 10-cm DuoFLEX array coils (MR Instruments, Minneapolis, MN, USA) placed at the sides of the pig head were used for receiving to improve the signal-to-noise ratio (SNR) over the brain. The MRI parameters used for pre- and post-imaging are summarized in Table 2. Before delivering histotripsy treatment, T2- and T2*-weighted MRI scans were obtained as a baseline for treatment outcome evaluation and used to locate the target via fiducial markers. On the basis of the fiducial markers attached to the array, the geometric focus of the array was identified on the MR images, and the pig was moved to ensure the geometric focus lay within the target volume for the maximal treatment efficacy. The orientation of the pig head was also adjusted to achieve unobstructed ultrasound propagation to the target through the craniotomy window. The following

Table 1. Treatment parameters

No.	Target location	Depth of target location (mm)	Aberration correction	p_- (MPa)	Planned volume (mm^3)
1	Right lateral ventricle	22	No	48.4	4.5 × 4.5 × 5
2	Left cingulate gyrus−corpus callosum	24	No	48.4	7.5 × 7.5 × 5
3	Midbrain	26	No	48.4	7.5 × 7.5 × 8
4	Thalamus and surrounding white matter	17	Yes	72	5.5 × 5.5 × 8
5	Cortical gray−white junction	8	Yes	72	7.5 × 7.5 × 5
6	Gray−white junction	8	Yes	72	4.5 × 4.5 × 5
7	Basal ganglia, peri-midline	25	Yes	72	4.5 × 4.5 × 2
8	deep white matter, external capsule	22	Yes	72	5.5 × 5.5 × 5

Table 2. Magnetic resonance imaging parameters used for pre- and post-treatment imaging

Type	Field of view (mm)	Slice thickness (mm)	TR (ms)	TE (ms)	Matrix width	NEX	Acquisition
T2	200–240	3	3532–4431	106–113	256–320	1–2	Pre, post and 2–4 h post for all pigs
T2*	200–240	3	325–350	10	256–320	0.5–1	Pre, post and 2–4 h post for all pigs
T1	220–245	1–3	2D: 3628– 3636 3D: 7.1–7.4	2D: 22– 23 3D: 2.9–3.0	260–300	0.5–1.5	Post and 2–4 h post for pigs 5 and 6; pre, post and 2–4 h post for pigs 7 and 8
T2 FLAIR	200–240	1–3	6332–13000	103–134	192–300	0.5–2	2 h post for pigs 2 and 4; post and 2–4 h post for pigs 1, 3, 5 and 6; pre, post and 2–4 h post for pigs 7 and 8
DWI	200–360	3	2000–6000	61–86	128	2–4	Post for pig 5 (b = 1000 s/mm^2); 1–3 h post for pigs 3, 4 and 6 (b = 1000 s/mm^2); pre, post and 2–4 h post for pigs 7 and 8 (b = 500 s/mm^2)
T2 3-D	160–256	0.8–3	3002–3952	89–143	232–384	1–2	Post and 1–4 h post for all pigs

DWI = diffusion-weighted imaging; NEX = number of excitations.

MRI sequences were acquired immediately after treatment and then again 2–4 h later before euthanizing the pig: T2-weighted, T2*-weighted, T2 FLAIR (fluid-attenuated inversion recovery), T1-weighted and diffusion-weighted imaging (DWI). T2* sequences, as a measure of iron and hemosiderin in the targeted brain tissue, can visualize blood product extravasation resulting from vascular damage, while the other sequences were chosen to visualize the histotripsy ablation-related tissue homogenization and the extent of resulting brain edema. The acquired MRI sequences were evaluated by a neurointerventionalist (board-certified neurodiagnostic radiologist) and a neurosurgeon to analyze the histotripsy treatment outcomes.

Targeting accuracy assessment

The targeting accuracy of tcMRgHt was assessed using the post-treatment T2- and T2*-weighted MRI. Because the treatment grid of the target volume was defined based on the fiducial markers in this study, the center of the targeted volume can be marked related to the locations of fiducial markers. In comparison, the center of the observed ablation zone on the corresponding MR slice indicated the actual center location of the treated zone. Thus, the Euclidean distance between the targeted center and the treated center was measured on the MR images to represent the focal shift during the treatment, as illustrated in Figure 2. Because the initial design of fiducial markers did not provide sufficient precision to help locate the target, a pair of new fiducial markers were fabricated and added into the transducer assembly after the first three pig treatments. Therefore, the targeting accuracy achieved in this study was evaluated by the mean and standard deviation of the focal shift distance for only the later five pigs (pigs 4 to 8) in the mediolateral (ML) and superior-to-inferior (SI) dimensions. The distance in the anterior-to-posterior (AP) dimension was not measured because the slice thickness was too large to provide the necessary precision.

Histological analysis

All animals were euthanized 2–4 h post-treatment. The pig heads were harvested and fixed in 10% buffered formalin solution for at least 7 d before removing the

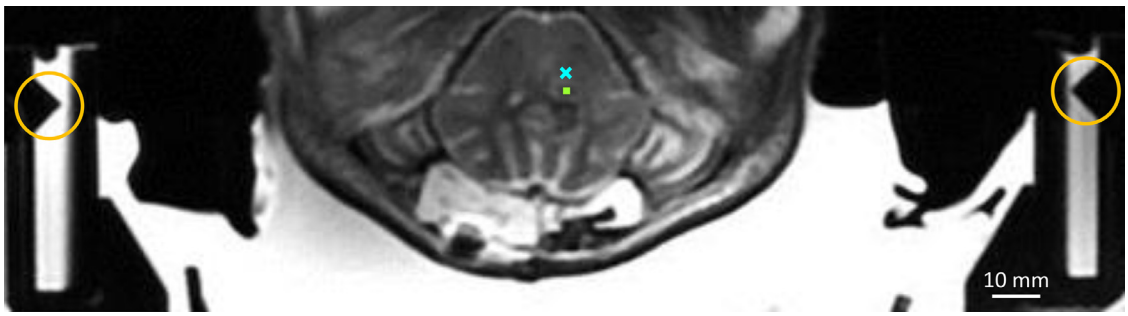

Fig. 2. Targeting accuracy measurement for pig 4 on a 2-h post-T2-weighted image. The fiducial markers attached to the array scaffold are shown as two triangular pointers (labeled in *yellow circles*) symmetrically located on the left and right sides. The center of the target zone is labeled with a *cyan* ×, whereas the center of the observed apparent ablation zone is labeled with a *green dot*. The targeting accuracy was then quantified as the distance between these two locations and can be decomposed into lateral and axial shifts.

brains. Then, the pig brains were sectioned around the location of tcMRgHt treatment based on the presentation of lesions on MRI and sliced every 1.5 mm in the coronal plane from anterior to posterior through the expected lesion volume. The brain sections were embedded in paraffin and stained with hematoxylin and eosin (H&E). A microscopic histological examination was performed by a neuropathologist for histopathological assessment.

Lesion size estimation

Lesion sizes were estimated on the H&E-stained sections with the largest lesion extent for each pig and the corresponding post-treatment MRI scans, represented by the maximum diameters of the lesion in the superior-to-inferior and mediolateral dimensions. For T2- and T2*-weighted MR images, the lesion size was measured by the diameters of the hyper-intense and hypo-intense regions, respectively. For histology, the lesion size was measured by the diameter of the region with homogenized acellular debris and red blood cells (RBCs), including the extended ischemic injuries observed at the boundaries of the lesions.

RESULTS

TcMRgHt treatment was performed successfully and confirmed by MRI for all eight pigs. The treatment zone was confirmed by histological examination for all pigs. All pigs tolerated both the surgical and ultrasound procedures without incident.

MRI evaluation

MR evidence of successful histotripsy ablation was observed on post-treatment scans for all pigs. Pre- and post-treatment images from one pig with the target in the deep brain (Fig. 3, pig 3) and one pig with the target in the shallow cortical region (Fig. 4, pig 6) are provided as examples. The treatment-associated contrasts on different types of post-treatment MRI scans are summarized in Table 3.

T2-Weighted MR images revealed hyper-intense histotripsy ablation zones compared with the surrounding untreated tissue, as the cavitation generated by histotripsy liquefied the tissue. These hyper-intense regions were confined within the targeted volume, with no significant brain edema outside the treated region (Fig. 3d, 3g). In pigs 2, 4 and 6, a central hypo-intense region surrounded by a hyper-intense boundary was observed at the treated volume immediately after the treatment (Fig. 4c). The central signal loss was attributed to acute local hemorrhage within the treatment zone and became less obvious after 2−4 h post-treatment, revealing a more homogeneous hyper-intense region at the targeted location (Fig. 4g). On T2 FLAIR images, the target areas also appeared hyper-intense, and hypo-intense regions were observed inside the target areas. The treatment-induced contrast was less visible on T2 FLAIR images than T2-weighted images.

On T2*-weighted images, the target area was evident as well-confined hypo-intense regions (Fig. 3e, 3h). For pigs 1 and 4, hypo-intense signals appeared inside or around the ventricles outside of the treatment grid, because cellular and non-cellular components of extravasated blood were present in the ventricles when the target zones included peri-ventricular regions. For pigs 5, 6 and 8, discrete mild hypo-intense regions were observed outside the target volume (Fig. 4d, 4h), which was likely owing to blood product extravasation from the damaged microvascular structures included in the treatment scan grid. Nevertheless, a comparison between the pre- and post-treatment images revealed no MRI-evident changes in the ultrasound beam path pre-focal or post-focal. The diffusion-weighted images were characterized primarily with dense hypo-intense regions at the treated locations (Fig. 3j), reviewing contrast similar to that of T2*-weighted images.

The target area appeared hypo-intense on T1-weighted images (Fig. 4f, 4j), suggesting increased fluid at the treated volume. Because the liquefied tissue debris, edema and hyperacute hemorrhage all appear hypo-intense on T1-weighted images, the T1-weighted images only confirmed the treatment but provided no further information on treatment outcomes.

Targeting accuracy

The distance between the center of the target region and the center of the observed ablation zone was calculated for five pigs (pigs 4−8) in the superior-to-inferior and mediolateral dimensions. On the basis of the post-treatment T2- and T2*-weighted images, the shift was measured to be 1.21 ± 0.96 mm in the mediolateral direction toward the right side of the transducer array, and 1.69 ± 1.38 mm axially in the pre-focal direction, resulting in a mean total shift of 2.3 mm and the largest total shift of 3.5 mm. The shift suggested that the location of the effective ablation was biased pre-focally and laterally. Among these five pigs, two were targeted in superficial locations (pigs 5 and 6, <12 mm from the brain surface) and three were targeted in deep locations (pigs 4, 7 and 8, >12 mm from the brain surface). We did not observe any differences in targeting accuracy in the deep versus superficial locations.

Histological evaluation

Histopathological lesions attributed to the histotripsy treatment were identified at targeted locations for all eight pigs. The size and location of the lesions shown

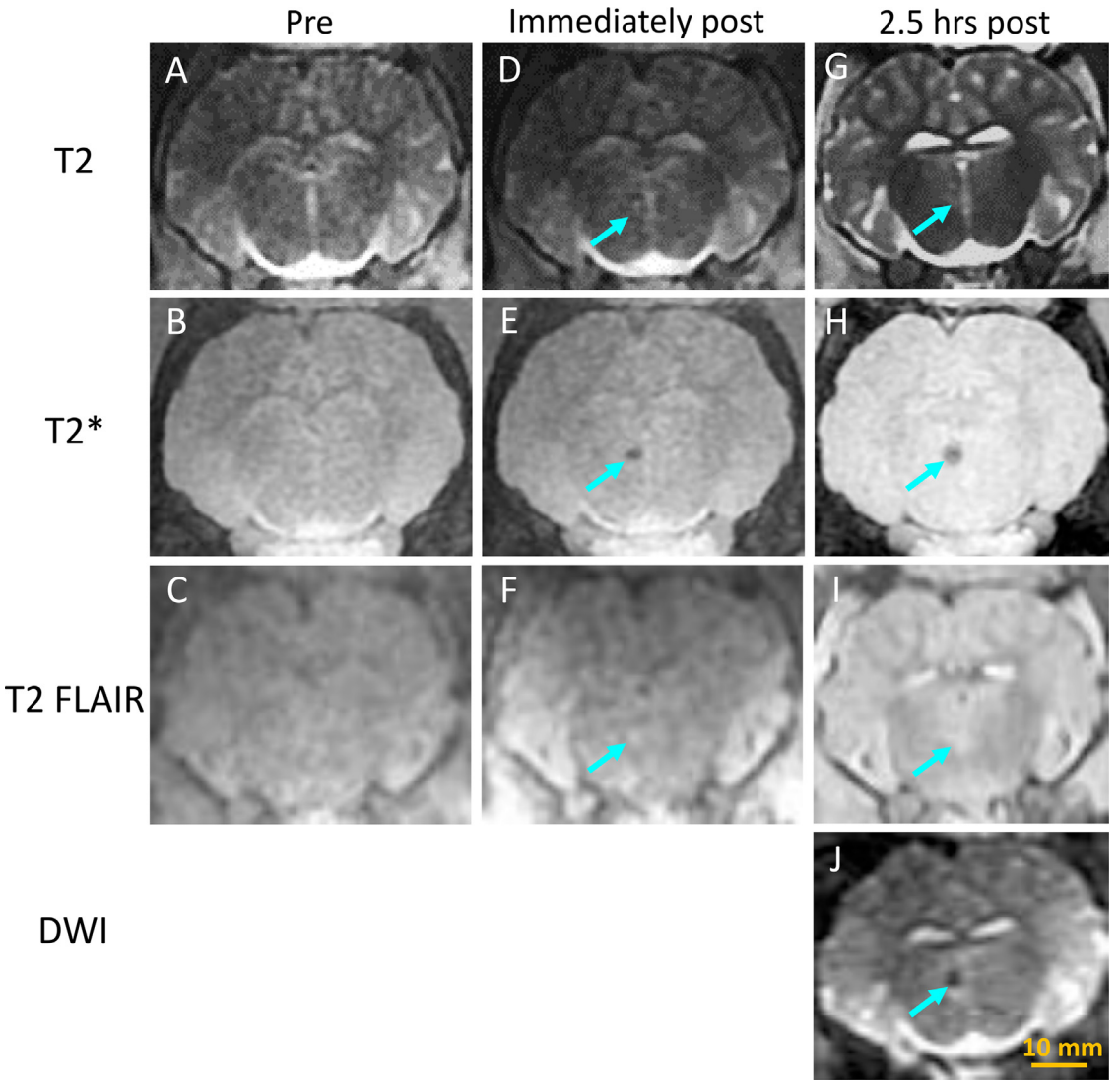

Fig. 3. Pre-treatment (a–c), immediately post-treatment (d–f) and 2.5-h post-treatment (g–j) magnetic resonance imaging MRI for pig 3 with the target in the midbrain. Top row (a, d, g): T2-Weighted; second row (b, e, h): T2*-weighted; third row (c, f, i): T2 fluid-attenuated inversion recovery (FLAIR); last row (j): diffusion-weighted imaging (DWI). The diffusion-weight scan was taken 2–4 h post-treatment only for this pig. The ablation zone is labeled by the *cyan arrow* on all post-treatment images.

on histology correlate well with the regions with intensity change on MRI, as illustrated in Figure 5.

Lesions were composed primarily of homogenized acellular debris and RBCs (Fig. 6a, 6b), with sharply defined boundaries of tissue disruption between damaged and intact tissues. Ischemic injuries were observed at the boundaries of the lesions, with shrunken neurons and axonal disruption extending $\leq$500 μm from the lesions' borders (Fig. 6c). There was no significant gyral edema or midline shifting related to the lesion. Tissues adjacent to lesions were unremarkable, with no evidence of secondary effects related to treatment. For pigs 5 and 6 with targets in the cortex, the presence of RBCs in the subarachnoid space was observed near ablation zones close to boundaries, but it remained well confined only to the area of treatment. Perilesional vacuolated neuropils were seen (Fig. 6d), consistent with acute edema at the target locations. Destruction of cells within the treatment volumes was apparent at all targets regardless of the target anatomical locations. There were no significant differences between the deep targets and superficial targets in terms of the lesion composition, sharpness of boundaries or generation of perilesional damage. Overall, the histological changes associated with histotripsy-generated lesions resemble those of a confined acute infarct.

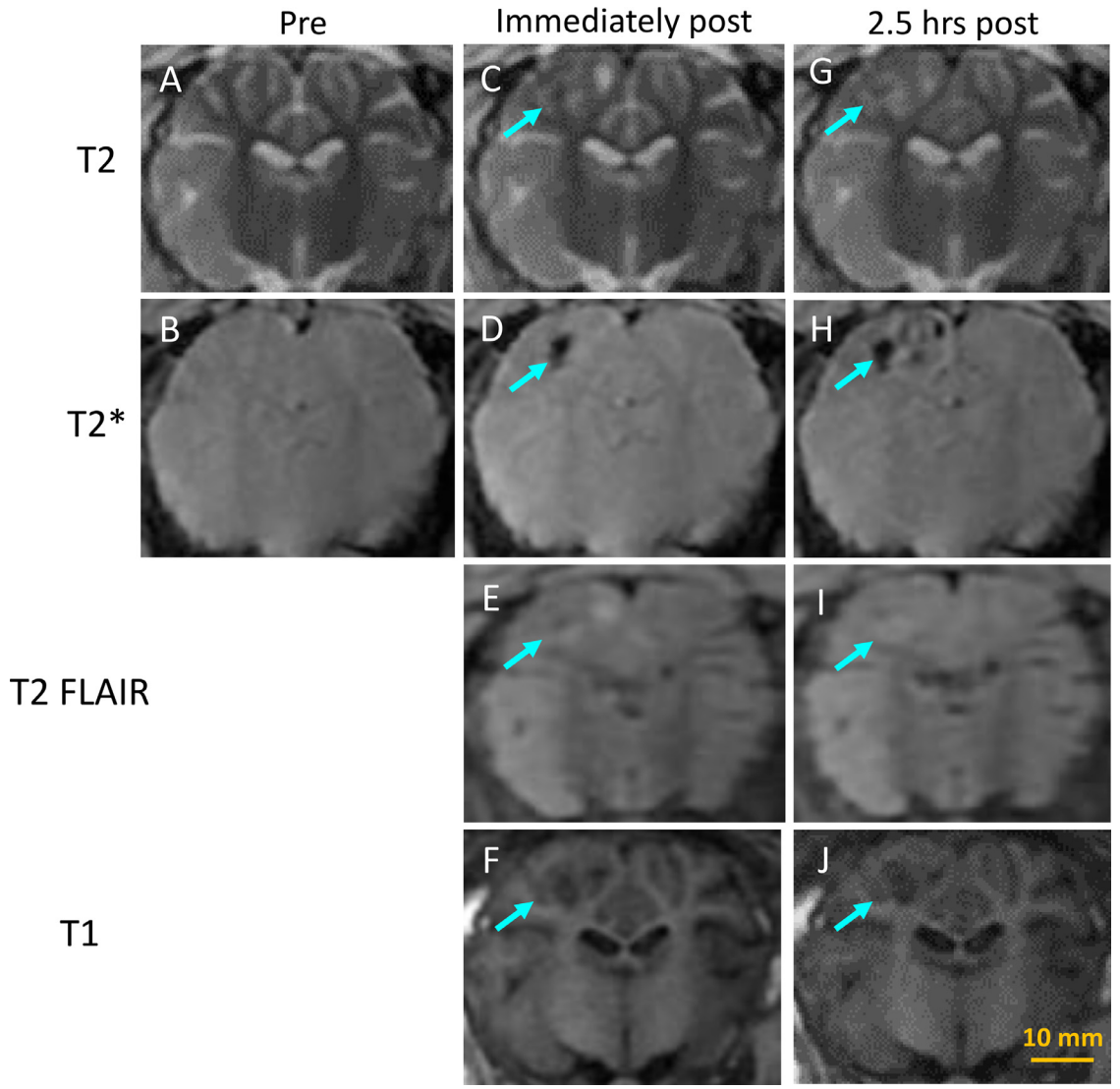

Fig. 4. Pre- (a, b), immediately post- (c–f) and 2.5-h post-treatment (g–j) magnetic resonance imaging for pig 6 with the target in the cortex. Top row (a, c, g): T2-weighted; second row (b, d, h): T2*-weighted; third row (e, i): T2 fluid-attenuated inversion recovery (FLAIR); last row (f, j): T1-weighted. The pre-treatment T2 FLAIR and T1-weight scans were not taken for this pig. The ablation zone is labeled by the cyan arrow on all post-treatment images.

Blood product extravasation outside the target volume was observed on histology from four pigs. The hemorrhage on the base of the brain of pig 2 (Fig. 8a) was caused by the RBCs from the treated zone flowing through the longitudinal fissure and, thus, was not associated with histotripsy damage. The blood products presented on the brain surface of pig 5 (Fig. 8b) were believed to be the upwelling of blood into the cranium as the planned treatment grid straddled multiple sulci. Discrete blood product extravasation was spotted outside the target volume in the brain of pig 4 (Fig. 8c) and pig 8 (Fig. 5c), which was likely affected by the disruption to the vasculature within the treated zone. The hemorrhagic risk and off-target damage associated with histotripsy lesions were not within the scope of this initial feasibility study, and future studies will be required to fully address this issue.

Lesion size estimation

The lesion sizes on histology and the post-treatment MRI scans are summarized in Figure 7. In general, the lesion sizes measured using T2*-weighted MR images and H&E-stained sections were slightly larger than those measured on corresponding T2-weighted MR images, although there were no statistically significant differences. This was expected as the T2*-weighted MRI and histology reveal the regions with blood product extravasation, which usually overestimate the underlying homogenized acellular debris. On both T2- and T2*-weighted images, the lesion

Table 3. Histotripsy-induced contrast on post-treatment MRI scans

Scan	Intensity changes induced by histotripsy treatment
T2	Hyper-intensity at the target zone indicated tissue liquefaction, and the central hypo-intense region within the target zone was owing to local hemorrhage immediately post-treatment.
T2*	Well-confined hypo-intense regions at the target location. Discrete mild hypo-intense regions outside the target volume were likely owing to blood product extravasation from the damaged microvascular structures included in the treatment grid.
T2 FLAIR	Like T2 but with lower contrast—the hyper-intense region indicates tissue liquefaction at the target volume, and the hypo-intense area inside the target area suggests acute local hemorrhage.
T1	The homogenous hypo-intense region indicates increased fluid, such as liquefied acellular debris and/or acute hemorrhage.
DWI	Hypo-intense at the target region with a *b* value of 500 or 1000 s/mm^2.

DWI = diffusion-weighted imaging.

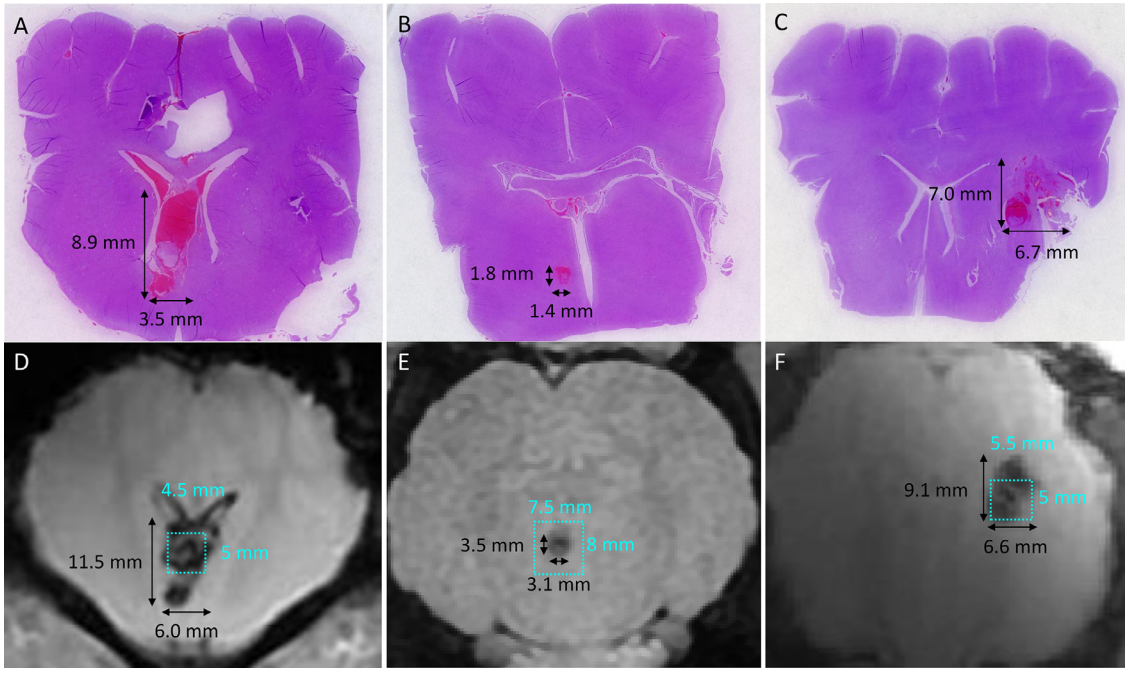

Fig. 5. Correlation between magnetic resonance imaging and histology from three pigs. Top row: Hematoxylin and eosin-stained pig brain sections revealing pathological lesions at targeted locations from pig 1 (a), pig 3 (b) and pig 8 (c). Bottom row: T2*-Weighted magnetic resonance images from each pig correspondingly. The measured dimensions of lesions were labeled in *black*, and the planned treatment zones were labeled with *cyan boxes*. It should be noted that for pig 3, the resulting ablation zone was smaller than the planned volume because part of the transducer was blocked by the remaining pig skull. The hemorrhage in ventricles for pig 3 was likely owing to tissue harvesting and was not associated with direct local histotripsy damage.

expanded during the 4-h time window post-treatment. Compared with the targeted size, the immediately post-treatment T2-weighted images seemed to offer a most conservative estimation for the size of the treated area, whereas the other measurements tended to overestimate the treated size in general.

In general, the measured lesion sizes matched the planned treatment sizes. There were no statistically significant differences between the measured lesion sizes and the planned treatment sizes. It should be noted that for pigs 2 and 3, the treated region was smaller than the planned volume because part of the transducer was blocked by the remaining pig skull and aberration correction was not used. These two pigs had the largest planned treatment size (8 mm in SI dimension, 7.5 mm in ML dimension); thus, the mean lesion sizes appeared to be smaller than the planned treatment sizes, with large standard deviations for the largest planned treatment size group (Fig. 7).

DISCUSSION

Here we presented the first study on the feasibility of using tcMRgHt treatment *in vivo* and highlighted the ability of histotripsy as a non-invasive and non-thermal treatment

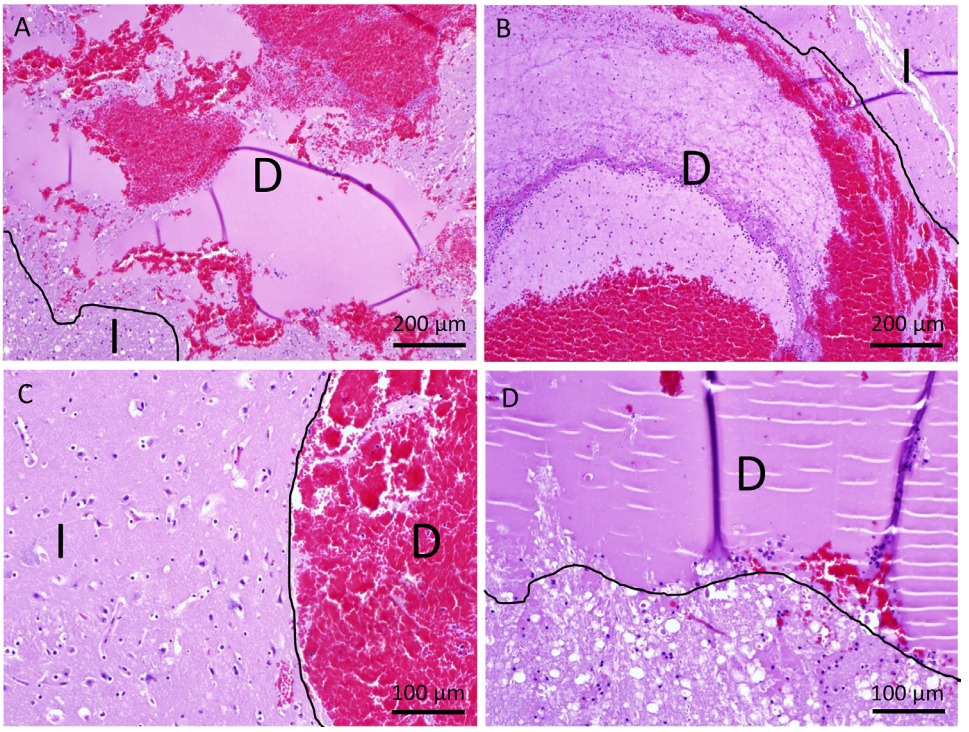

Fig. 6. Histotripsy lesions on hematoxylin and eosin-stained sections. The boundary between treated and untreated regions is labeled with a curved line in *black*. The treated region was composed primarily of disrupted (D) acellular debris and red blood cells, while the neurons remained intact (I) in the untreated region. (a) Liquefied tissue surrounded by blood products within the treatment area from pig 4. (b) Homogenized acellular debris and blood product in the treated region from pig 8. (c) The interface between disrupted and intact regions revealing a sharp boundary around the hemorrhage area from pig 4, with shrunk neurons observed outside the lesions' borders. (d) Vacuolated brain tissue in the treated region from pig 8 revealing macrophages with bubbly cytoplasm.

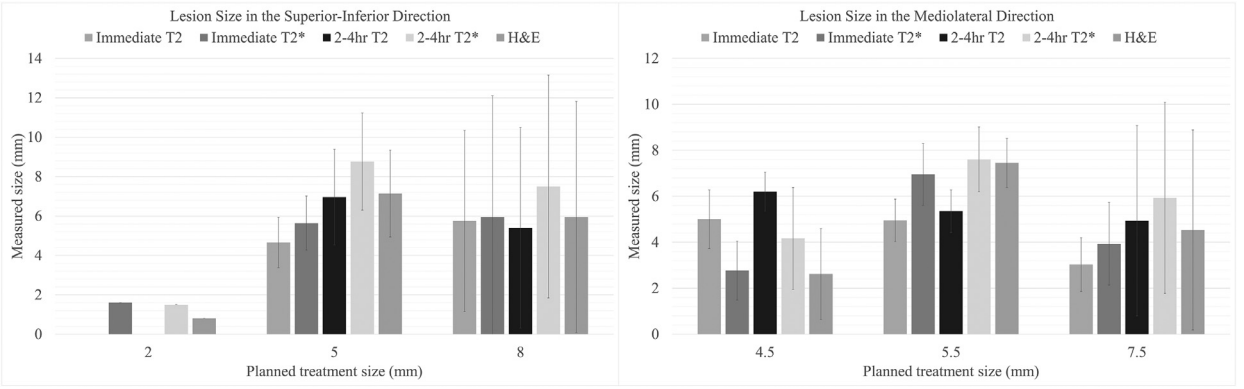

Fig. 7. Sizes of lesions (vertical axis) on post-treatment magnetic resonance imaging and histology in the superior-to-inferior and mediolateral directions compared with the planned treatment sizes (horizontal axis). H&E = hematoxylin and eosin.

option for brain disorders. MRI and histological analysis indicated that well-demarcated lesions can be produced with a minimal area of surrounding injury and the presence of RBCs within the targeted region after liquefaction of cerebral tissue. While the presence of RBCs within the ventricle and subarachnoid space was observed when lesions incorporated sulci or the periventricular region, it was limited in extent and confined to the treatment area. Histopathological findings 2−4 h after tcMRgHt treatment revealed homogenized acellular debris and an abundance of macrophages within the treated area. The edema response to histotripsy ablation in the brain was generally minimal,

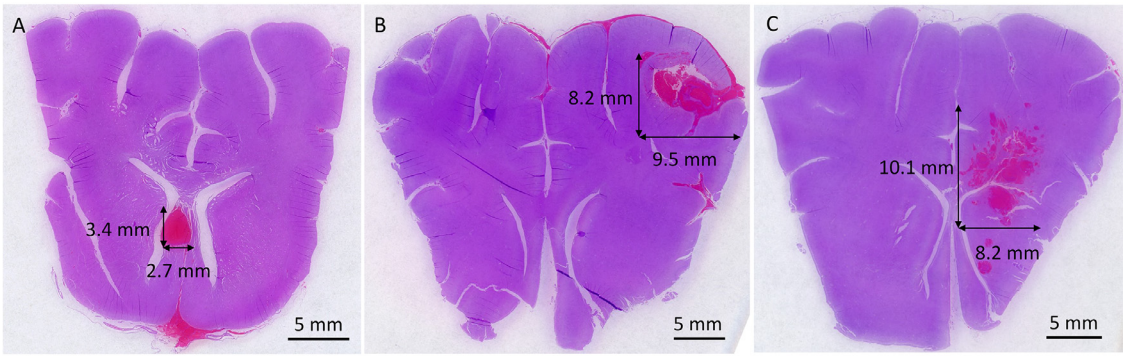

Fig. 8. Hematoxylin and eosin-stained sections with blood product extravasation outside the target volume. (a) Hemorrhage was observed on the base of the brain of pig 2. (b) Blood products were observed on the brain surface of pig 5. (c) Discrete blood product extravasation was spotted outside the target volume in the brain of pig 4. The identified lesions at the target zone are labeled with *black arrows* and the measured size for each case.

extending <1 mm from the boundaries of the ablation zones.

The histotripsy ablation zone appeared hypo-intense on post-treatment diffusion-weighted images. Histotripsy liquefies the target tissue, increasing the local diffusivity in the target volume, resulting in a signal loss on diffusion-weighted images. However, it should be noted that the diffusion-weighted images possess both T2 weighting and diffusion weighting. Therefore, lesions with very short T2 (or T2*) values may reduce the signal intensity in the DWI scans, potentially destroying pure diffusion contrast and appearing artificially hypo-intense, known as the "T2-blackout" phenomenon. As illustrated in Figure 3, the location of hypo-intense lesions on DWI correlates very well with the location of hypo-intense lesions on T2*-weighted images, suggesting that the intensity changes on DWI were very likely owing to a combination of blood product extravasation and increased diffusion at the target. In such cases, apparent diffusion coefficient (ADC) maps may need to be acquired along with T2- and T2*-weighted images to understand the underlying pathological conditions at the hypo-intense lesions on DWI, as reported in previous studies on MRgFUS (Zhong et al. 2019; Allen et al. 2021) and *in vitro* histotripsy (Allen et al. 2017).

For the present study, targeting was achieved based on fiducial markers only. Thus, the targeting accuracy here is likely a worst-case scenario of tcMRgHt treatment. The analysis of targeting accuracy revealed that the location of the effective ablation was biased prefocally and laterally, which might be attributed to systematic errors from registering the fiducial markers on the MR images owing to the limited slice thickness and image resolution.

The major limitations in this study are the lack of MR-based pre-treatment targeting and treatment monitoring. Ideally, the location of the ultrasound beam focus through the skull needs to be precisely visualized on MRI. MR thermometry is capable of measuring temperature changes of the focal region in real time, making it a favorable tool to verify, monitor and adjust the focal location in tcMRgFUS (Chauvet et al. 2013; Moser et al. 2013; Ellens et al. 2015; Gallay et al. 2019). It is possible to apply ultrasound to produce low heating and use MR thermometry for histotripsy pre-treatment targeting. MR-Acoustic radiation force impulse (ARFI) imaging (McDannold and Maier 2008; Hertzberg et al. 2010; Kaye et al. 2011; Kaye and Pauly 2013) is another alternative approach for MR-based histotripsy pre-treatment targeting. It is also possible to develop diffusion-weighted MRI to image cavitation-induced motion for treatment monitoring. Previous studies have found that specialized MRI sequences can visualize histotripsy-induced cavitation and *in vitro* tissue fractionation (Allen et al. 2015, 2016). Though attempts have been made to adapt this method for our *in vivo* pig treatment, technical challenges remain to be solved, including the limits on spatial resolution and signal-to-noise ratio of the 3-T whole-body scanner, the complexity of *in vivo* tissue contrast, and the sensitivity that is required to detect the millimeter-level cavitation events in a relatively large field of view of about 200 mm. Further investigations are currently ongoing to develop the MR-based pre-treatment targeting and treatment monitoring for histotripsy.

Hydrophone-based aberration correction was applied herein to compensate for the phase variance introduced by the human calvarium, which is not compatible with non-invasive brain therapy. The phase delays were only calculated from hydrophone measurements at the geometric focus of the array and applied at all steering locations, which might not have efficiently compensated for the aberration at all steering locations.

In addition, this method did not take into consideration any aberration induced by the soft tissue in the ultrasound beam path (variation between saline and brain). For optimal re-focusing, non-invasive *in vivo* aberration correction could be implemented via simulation (Jones and Hynynen 2015; Leung et al. 2019), MR-ARFI (Vyas et al. 2014; Liu et al. 2015) or analytical CT-based methods (Aubry et al. 2003; Jones and Hynynen 2015; Jones et al. 2015). These strategies will be investigated in future studies along with the beam focus visualization to improve treatment precision and efficiency.

Though a craniotomy was performed in this porcine study, it was only necessary for the porcine treatment because of the geometric differences between the pig skull and the human skull. For clinical procedures, a craniotomy would not be required because the reduced human skull thickness and more spherical shape allow for transcranial histotripsy treatment. In addition, the locations of populated transducers and the geometry of supporting structures used in this study were also designed based on the geometry of the pig head. For future clinical tcMRgHt systems, we envision a full hemispherical transducer array to be integrated with a helmet-shaped acoustic coupler to couple the sound from the transducer array to the patient's head. An MR-conditional motorized positioner can also be integrated into future clinical systems to alleviate the positioning difficulties we have experienced in this study and facilitate the treatment. These factors will be taken into consideration and carefully addressed in future system design.

In this study, tcMRgHt was applied to the *in vivo* normal swine brain. In liver tumor and melanoma models, histotripsy has been reported to reduce local tumor progression, stimulate intra-tumoral infiltration of innate and adaptive immune cell populations and cause an abscopal effect with inhibited growth of the contralateral untreated tumor as well as pulmonary metastases (Qu et al. 2020; Worlikar et al. 2020). Future studies will be needed to investigate the capabilities of tcMRgHt in the treatment of brain tumors and other brain disorders in disease models. Moreover, as this study is only an acute study, additional preclinical studies will need to be conducted to investigate and confirm the subacute and chronic safety, particularly on the subacute edema and inflammation at least 48 h post-treatment, as well as long term inflammation-based healing and encephalomalacia.

CONCLUSIONS

This study was the first to determine the *in vivo* feasibility of using tcMRgHt in the pig brain through an excised human skull. With a recently developed MR-compatible transcranial histotripsy system, we successfully treated brain volume targets in eight pigs through the human calvarium. The MR-evident lesions were well confined within the targeted volume. Histology revealed tissue homogenization within the ablation zones with a sharp demarcation between damaged and intact tissue, which correlated well to the identified treatment zones on MRI. Minimal injury in the 1 mm of cerebra tissue surrounding the target was observed, without any significant edema, hemorrhage or damage outside the target. These results provide important evidence to support that tcMRgHt offers a non-invasive treatment option for brain applications and lays the groundwork for the use of tcMRgHt for brain surgical applications.

Acknowledgments—This work was funded by the Focused Ultrasound Foundation and National Institutes of Health (R01-EB028309 and R01-NS108042). The authors thank Dr. Tyler I. Gerhardson and Aleksandra Rakic from Histosonics Inc. for helping with the design of the transducer scaffold and the pig V-tray.

Conflict of interest disclosure—Z.X. and T.H. have financial and/or other relationships with HistoSonics Inc. The University of Michigan has a financial interest in Histosonics Inc.

REFERENCES

Alkins R, Huang Y, Pajek D, Hynynen K. Cavitation-based third ventriculostomy using MRI-guided focused ultrasound: Laboratory investigation. J Neurosurg 2013;119:1520–1529.

Allen SP, Hall TL, Cain CA, Hernandez-Garcia L. Controlling cavitation-based image contrast in focused ultrasound histotripsy surgery. Magn Reson Med 2015;73:204–213.

Allen SP, Hernandez-Garcia L, Cain CA, Hall TL. MR-based detection of individual histotripsy bubble clouds formed in tissues and phantoms. Magn Reson Med 2016;76:1486–1493.

Allen SP, Vlaisavljevich E, Shi J, Hernandez-Garcia L, Cain CA, Xu Z, Hall TL. The response of MRI contrast parameters in in vitro tissues and tissue mimicking phantoms to fractionation by histotripsy. Phys Med Biol 2017;62:7167–7180.

Allen SP, Prada F, Xu Z, Gatesman J, Feng X, Sporkin H, Gilbo Y, DeCleene S, Pauly KB, Meyer CH. A preclinical study of diffusion-weighted MRI contrast as an early indicator of thermal ablation. Magn Reson Med 2021;85:2145–2159.

Arvanitis CD, Vykhodtseva N, Jolesz F, Livingstone M, McDannold N. Cavitation-enhanced nonthermal ablation in deep brain targets: Feasibility in a large animal model. J Neurosurg 2016;124:1450–1459.

Aubry JF, Tanter M. MR-Guided transcranial focused ultrasound. Adv Exp Med Biol 2016;880:97–111.

Aubry JF, Tanter M, Pernot M, Thomas JL, Fink M. Experimental demonstration of noninvasive transskull adaptive focusing based on prior computed tomography scans. J Acoust Soc Am 2003;113:84–93.

Behrens S, Daffertshofer M, Spiegel D, Hennerici M. Low-frequency, low-intensity ultrasound accelerates thrombolysis through the skull. Ultrasound Med Biol 1999;25:269–273.

Chauvet D, Marsac L, Pernot M, Boch AL, Guillevin R, Salameh N, Souris L, Darrasse L, Fink M, Tanter M, Aubry JF. Targeting accuracy of transcranial magnetic resonance-guided high-intensity focused ultrasound brain therapy: A fresh cadaver model: Laboratory investigation. J Neurosurg 2013;118:1046–1052.

Coluccia D, Fandino J, Schwyzer L, O'Gorman R, Remonda L, Anon J, Martin E, Werner B. First noninvasive thermal ablation of a brain tumor with MR-guided focused ultrasound. J Ther Ultrasound 2014;2:17.

Elias WJ, Huss D, Voss T, Loomba J, Khaled M, Zadicario E, Frysinger RC, Sperling SA, Wylie S, Monteith SJ, Druzgal J, Shah BB, Harrison M, Wintermark M. A pilot study of focused ultrasound thalamotomy for essential tremor. N Engl J Med 2013;369:640–648.

Ellens NPK, Kobelevskiy I, Chau A, Waspe AC, Staruch RM, Chopra R, Hynynen K. The targeting accuracy of a preclinical MRI-guided focused ultrasound system. Med Phys 2015;42:430–439.

Fasano A, De Vloo P, Llinas M, Hlasny E, Kucharczyk W, Hamani C, Lozano AM. Magnetic resonance imaging-guided focused ultrasound thalamotomy in Parkinson tremor: Reoperation after benefit decay. Mov Disord 2018;33:848–849.

Federau C, Goubran M, Rosenberg J, Henderson J, Halpern CH, Santini V, Wintermark M, Butts Pauly K, Ghanouni P. Transcranial MRI-guided high-intensity focused ultrasound for treatment of essential tremor: A pilot study on the correlation between lesion size, lesion location, thermal dose, and clinical outcome. J Magn Reson Imaging 2018;48:58–65.

Gallay MN, Moser D, Jeanmonod D. Safety and accuracy of incisionless transcranial MR-guided focused ultrasound functional neurosurgery: Single-center experience with 253 targets in 180 treatments. J Neurosurg 2019;130:1234–1243.

Gerhardson T, Sukovich JR, Pandey AS, Hall TL, Cain CA, Xu Z. Effect of frequency and focal spacing on transcranial histotripsy clot liquefaction, using electronic focal steering. Ultrasound Med Biol 2017;43:2302–2317.

Hertzberg Y, Volovick A, Zur Y, Medan Y, Vitek S, Navon G. Ultrasound focusing using magnetic resonance acoustic radiation force imaging: Application to ultrasound transcranial therapy. Med Phys 2010;37:2934–2942.

Ji R, Smith M, Niimi Y, Karakatsani ME, Murillo MF, Jackson-Lewis V, Przedborski S, Konofagou EE. Focused ultrasound enhanced intranasal delivery of brain derived neurotrophic factor produces neurorestorative effects in a Parkinson's disease mouse model. Sci Rep 2019;9:19402.

Jones RM, Hynynen K. Comparison of analytical and numerical approaches for CT-based aberration correction in transcranial passive acoustic imaging. Phys Med Biol 2015;61:23–36.

Jones RM, O'Reilly MA, Hynynen K. Experimental demonstration of passive acoustic imaging in the human skull cavity using CT-based aberration corrections. Med Phys 2015;42:4385–4400.

Kaye EA, Pauly KB. Adapting MRI acoustic radiation force imaging for in vivo human brain focused ultrasound applications. Magn Reson Med 2013;69:724.

Kaye EA, Chen J, Pauly KB. Rapid MR-ARFI method for focal spot localization during focused ultrasound therapy. Magn Reson Med 2011;65:738–743.

Khokhlova VA, Fowlkes JB, Roberts WW, Schade GR, Xu Z, Khokhlova TD, Hall TL, Maxwell AD, Wang YN, Cain CA. Histotripsy methods in mechanical disintegration of tissue: Towards clinical applications. Int J Hyperthermia 2015;31:145–162.

Kim Y, Hall T, Xu Z, Cain C. Transcranial histotripsy therapy: A feasibility study. IEEE Trans Ultrason Ferroelectr Freq Control 2014;61:582–593.

Leung SA, Webb TD, Bitton RR, Ghanouni P, Butts Pauly K. A rapid beam simulation framework for transcranial focused ultrasound. Sci Rep 2019;9:1–11.

Lipsman N, Schwartz ML, Huang Y, Lee L, Sankar T, Chapman M, Hynynen K, Lozano AM. MR-guided focused ultrasound thalamotomy for essential tremor: A proof-of-concept study. Lancet Neurol 2013;12:462–468.

Lipsman N, Meng Y, Bethune AJ, Huang Y, Lam B, Masellis M, Herrmann N, Heyn C, Aubert I, Boutet A, Smith GS, Hynynen K, Black SE. Blood–brain barrier opening in Alzheimer's disease using MR-guided focused ultrasound. Nat Commun 2018;9:1–8.

Liu N, Liutkus A, Aubry JF, Marsac L, Tanter M, Daudet L. Random calibration for accelerating MR-ARFI guided ultrasonic focusing in transcranial therapy. Phys Med Biol 2015;60:1069–1085.

Lu N, Hall TL, Choi D, Gupta D, Daou BJ, Sukovich JR, Fox A, Gerhardson TI, Pandey AS, Noll DC, Xu Z. Transcranial MR-guided histotripsy system. IEEE Trans Ultrason Ferroelectr Freq Control 2021;68:2917–2929.

Lundt JE, Allen SP, Shi J, Hall TL, Cain CA, Xu Z. Non-invasive, rapid ablation of tissue volume using histotripsy. Ultrasound Med Biol 2017;43:2834–2847.

Martin E, Jeanmonod D, Morel A, Zadicario E, Werner B. High-intensity focused ultrasound for noninvasive functional neurosurgery. Ann Neurol 2009;66:858–861.

McDannold N, Maier SE. Magnetic resonance acoustic radiation force imaging. Med Phys 2008;35:3748–3758.

McDannold N, Clement G, Black P, Jolesz F, Hynynen K. Transcranial MRI-guided focused ultrasound surgery of brain tumors: Initial findings in three patients. Neurosurgery 2010;66:323–332.

Monteith SJ, Kassell NF, Goren O, Harnof S. Transcranial MR-guided focused ultrasound sonothrombolysis in the treatment of intracerebral hemorrhage. Neurosurg Focus 2013;34:E14.

Moser D, Zadicario E, Schiff G, Jeanmonod D. MR-Guided focused ultrasound technique in functional neurosurgery: Targeting accuracy. J Ther Ultrasound 2013;1:1–10.

Parsons JE, Cain CA, Abrams GD, Fowlkes JB. Pulsed cavitational ultrasound therapy for controlled tissue homogenization. Ultrasound Med Biol 2006;32:115–129.

Pulkkinen A, Huang Y, Song J, Hynynen K. Simulations and measurements of transcranial low-frequency ultrasound therapy: Skull-base heating and effective area of treatment. Phys Med Biol 2011;56:4661–4683.

Qu S, Worlikar T, Felsted AE, Ganguly A, Beems MV, Hubbard R, Pepple AL, Kevelin AA, Garavaglia H, Dib J, Toma M, Huang H, Tsung A, Xu Z, Cho CS. Non-thermal histotripsy tumor ablation promotes abscopal immune responses that enhance cancer immunotherapy. J Immunother Cancer 2020;8 e000200.

Sukovich JR, Xu Z, Kim Y, Cao H, Nguyen TS, Pandey AS, Hall TL, Cain CA. Targeted lesion generation through the skull without aberration correction using histotripsy. IEEE Trans Ultrason Ferroelectr Freq Control 2016;63:671–682.

Sukovich JR, Cain CA, Pandey AS, Chaudhary N, Camelo-Piragua S, Allen SP, Hall TL, Snell J, Xu Z, Cannata JM, Teofilovic D, Bertolina JA, Kassell N, Xu Z. In vivo histotripsy brain treatment. J Neurosurg 2019;131:1331–1338.

Vlaisavljevich E, Kim Y, Allen S, Owens G, Pelletier S, Cain C, Ives K, Xu Z. Image-guided non-invasive ultrasound liver ablation using histotripsy: Feasibility study in an in vivo porcine model. Ultrasound Med Biol 2013;39:1398–1409.

Vyas U, Kaye E, Pauly KB. Transcranial phase aberration correction using beam simulations and MR-ARFI. Med Phys 2014;41 032901.

Wang TY, Xu Z, Winterroth F, Fowlkes JB, Hall TL, Roberts WW, Rothman ED, Cain CA. Quantitative ultrasound backscatter for pulsed cavitational ultrasound therapy—Histotripsy. IEEE Trans Ultrason Ferroelectr Freq Control 2009;56:995–1005.

Worlikar T, Mendiratta-Lala M, Vlaisavljevich E, Hubbard R, Shi J, Hall TL, Cho CS, Lee FT, Greve J, Xu Z. Effects of histotripsy on local tumor progression in an in vivo orthotopic rodent liver tumor model. BME Front 2020;2020 9830304.

Xu Z, Ludomirsky A, Eun LY, Hall TL, Tran BC, Fowlkes JB, Cain CA. Controlled ultrasound tissue erosion. IEEE Trans Ultrason Ferroelectr Freq Control 2004;51:726.

Xu Z, Carlson C, Snell J, Eames M, Hananel A, Lopes MB, Raghavan P, Lee CC, Yen CP, Schlesinger D, Kassell NF, Aubry JF, Sheehan J. Intracranial inertial cavitation threshold and thermal ablation lesion creation using MRI-guided 220-kHz focused ultrasound surgery: Preclinical investigation. J Neurosurg 2015;122:152–161.

Zhong J, Waspe AC, Looi T, Piorkowska K, Hawkins C, Drake JM, Hodaie M. Acute MR-guided high-intensity focused ultrasound lesion assessment using diffusion-weighted imaging and histological analysis. Front Neurol 2019;10:1069.